

Phase-resolved observations of optical pulse propagation in chip-scale silicon nanowires

Matthew D. Marko,^{1,2,a)} Xiujuan Li,³ Jiangjun Zheng,¹ Jiali Liao,³ Mingbin Yu,⁴ Guo-Qiang Lo,⁴ Dim-Lee Kwong,⁴ Chad A. Husko,⁵ and Chee Wei Wong^{1,a)}

¹Optical Nanostructures Laboratory, Columbia University, New York, New York 10027, USA

²Navy Air Warfare Center Aircraft Division (NAWCAD), Joint Base McGuire-Dix-Lakehurst, Lakehurst New Jersey 08733, USA

³Science College, National University of Defense Technology, Changsha, Hunan 410073, China

⁴The Institute of Microelectronics, 11 Science Park Road, Singapore Science Park II, Singapore

⁵Center for Ultrahigh bandwidth Devices for Optical Systems (CUDOS), School of Physics, University of Sydney, Australia

(Received 2 February 2013; accepted 21 April 2013; published online 8 July 2013)

We report phase-resolved temporal measurements of picosecond pulse propagation in silicon chip-scale nanowire waveguides. The nonlinear ultrafast phenomena are examined experimentally with frequency-resolved optical gating and numerically with nonlinear Schrödinger pulse modeling. Pulse broadening and higher-order pulse splitting were observed experimentally and matched remarkably with numerical predictions. The contributions of self-phase modulation and group velocity dispersion, as well as two-photon absorption, free-carrier dispersion, and absorption, are described and discussed, in support of chip-scale nonlinear signal processing and ultrafast processes. © 2013 Author(s). All article content, except where otherwise noted, is licensed under a Creative Commons Attribution 3.0 Unported License. [<http://dx.doi.org/10.1063/1.4813140>]

Recently, ultrafast optical soliton dynamics¹ have been advanced in semiconductor chip-scale optoelectronics, such as in silicon^{2–6} or in Gallium Indium Phosphide (GaInP) waveguides with temporal autocorrelation measurements and nonlinear pulse compression to 580-fs at low pulse energies in the range of 10-pJ.¹ In addition to intensity-based correlation measurements, these optical solitons have also been examined on-chip with spectral measurements^{7–10} with rigorously engineered dispersion,^{11–13} including slow-light Cerenkov-like radiation with self-frequency shift and soliton-radiation locking.¹⁴

Here we report phase-resolved measurements of optical pulse propagation in silicon on-chip waveguides, enabled by frequency-resolved optical gating (FROG). FROG has the advantage when studying ultrafast pulses to retrieve both the temporal pulse amplitude and the temporal phase of the output of an optical waveguide;¹⁵ this is in contrast with traditional autocorrelation that only gives an approximation of the pulse temporal duration. The relative contributions of group velocity dispersion (GVD) and third-order nonlinear processes such as self-phase modulation (SPM), two-photon absorption (TPA), free-carrier dispersion and absorption (FCA) are examined through FROG and nonlinear Schrödinger modeling, with aggregate behavior matching well with the experimental observations.

Figure 1 illustrates the scanning electron micrograph (SEM) of the 4- μm silicon channel (nanowire) waveguides examined in this study. The waveguides are fabricated by deep-ultraviolet lithography on SOITEC Unibond wafers, with 450-nm by 250-nm cross-section. Input-output coupling for the low-energy pulses is enhanced by oxide-cladded

inverse taper couplers on the silicon microchip fabricated at the Institute of Microelectronics in Singapore. Free-space coupling with objective lens (numerical aperture of 0.3) is performed, with typical total input-chip-output coupling losses between 10 and 13-dB. A half-wave plate and linear polarizer pair controls the pulse energy and ensures transverse-electric polarization is coupled onto the semiconductor chip.

To measure the phase of the ultrafast optical pulses, we build a FROG apparatus^{3,16–18} as illustrated in Figure 1(b), with a sensitivity of 0.18 mW² that could measure pulse energies down to 80 fJ. A second-harmonic-based optical gating was built, coupled to a high-resolution Horiba spectrometer (1000 M-Series II) with cryogenic back-illumination deep-depletion CCD detector in a 1024 \times 256 silicon array. With this sensitivity, the FROG was able to directly detect the second-harmonic of the short pulses after the chip without requiring erbium fiber amplifiers, which could distort the pulse characteristics. The input source is a tunable mode-locked fiber laser (PolarOnyx Saturn series), with near-transform-limited 2.3 ps pulses, averaged pulse energies at 600-pJ, 39.11-MHz repetition rates, and tunable wavelength range from 1536 to 1560-nm. The input linear polarization is mapped with a polarization controller at the input, to ensure consistent polarization in the series of measurements.

Figure 1(c) shows an example 2D frequency-time FROG spectrogram of the input pulse centered at 1560-nm, with the retrieved phase (solid green) and temporal intensity pulse-width (dashed blue) illustrated in the inset. The spectral width of this pulse is near-transform-limited at 1-nm and confirmed with an optical spectrum analyzer for consistency. The blue-side of the pulse shows a dual side-lobe temporal character from the pulse central region (also illustrated in inset), due to noise inherent to the mode-locked laser. In this

^{a)}Electronic addresses: matthew.marko@navy.mil and cww2104@columbia.edu

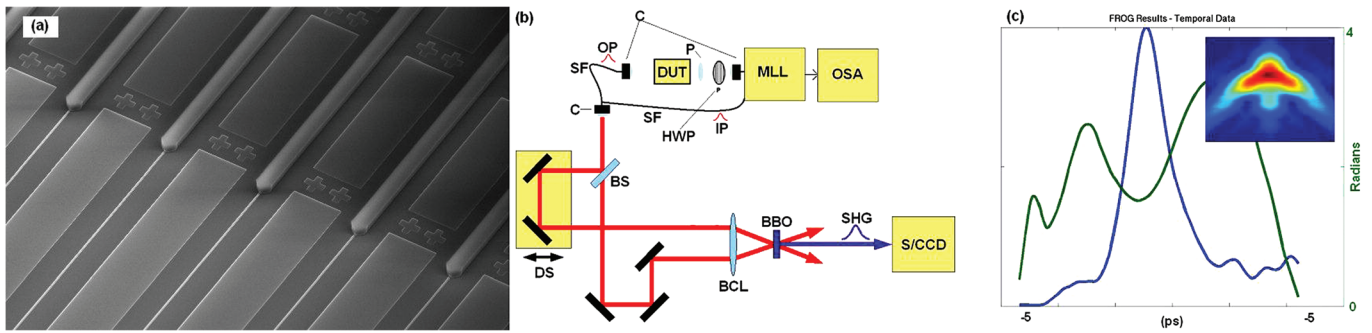


FIG. 1. (a) Example scanning electron micrograph of chip-scale silicon channel waveguide examined in this study. (b) Second harmonic FROG with cryogenic spectrometer for detection level at about 80-fJ, where C = Optical Collimator, DUT = Device Under Test, P = Polarizer, HWP = Half Wave Plate, IP = Input Pulse, OP = Output Pulse, MLL = Mode Locked Laser (39.11 MHz), OSA = Optical Spectrum Analyzer, SF = Short Fiber, BS = 50/50 Beam Splitter, DS = Delay Stage, BCL = Bi-Convex Lens, BBO = Beta Barium Borate crystal, SHG = Second Harmonic Generation, and S/CCD = Spectrometers with a liquid-nitrogen-cooled CCD camera. (c) Temporal intensity pulsewidth (blue) and example retrieved phase (green), of the laser input pulse. Inset: Example 2D spectrogram.

particular instance, the retrieved phase shows a standard deviation of 0.1π within the temporal pulse central region.

Figure 2 illustrates example 2D FROG spectrograms of the output pulses from the chip-scale waveguide with an estimated input pulse energy of 40 pJ, for tuned center wavelengths from 1536 to 1560 nm. In this case, each measurement is performed at 600-pJ input pulse energies, output from the fiber laser. In addition, the retrieved FROG error, in the 2D phase-retrieval solution and convergence, is determined to be 2% or less for each of the datasets reported here, and confirming the alignment of the setup. More involved techniques¹⁹ can also provide clarification on the uncertainty in the measured pulse intensity and phase in the presence of noise and ambiguity.

We highlight the retrieved pulse character for two example wavelengths (1542-nm and 1544-nm) with increasing pulse energies in Figure 3. Coupled input pulse energies from 200-fJ to 40-pJ are examined (estimated at the waveguide input, with

12-dB loss between laser output and waveguide input). With increasing pulse energy, pulse broadening from TPA was observed with a broadening factor ($\chi_b = T_{FWHM,out}/T_{FWHM,in}$) of 2.5 for 1542-nm at 40-pJ. For 1538-nm, χ_b is almost 3 at 40-pJ. At larger pulse energies, the SPM²⁰ is observed to be limited by TPA in the silicon²¹ waveguides. Because of the relative time and direction-of-time ambiguity in the FROG setup, in Figures 3(a) and 3(b), the pulses are each centered at zero relative time and the time-reversed solution plots chosen for reasonable continuity in temporal features for increasing pulse energies.

In Figure 3(c), we next illustrate the reconstructed phase (green solid line) for different pulses energies at 1544-nm. The relative phases are all fairly uniform with a phase standard deviation ranging from 0.05π (low energy pulses) to 0.18π (high energy pulses) in the full-width half-maximum (FWHM) of the pulsewidth (T_{FWHM}). Compared to the 1-pJ scenario, the intensity pulsewidth (blue solid line) is broadened at 5-pJ

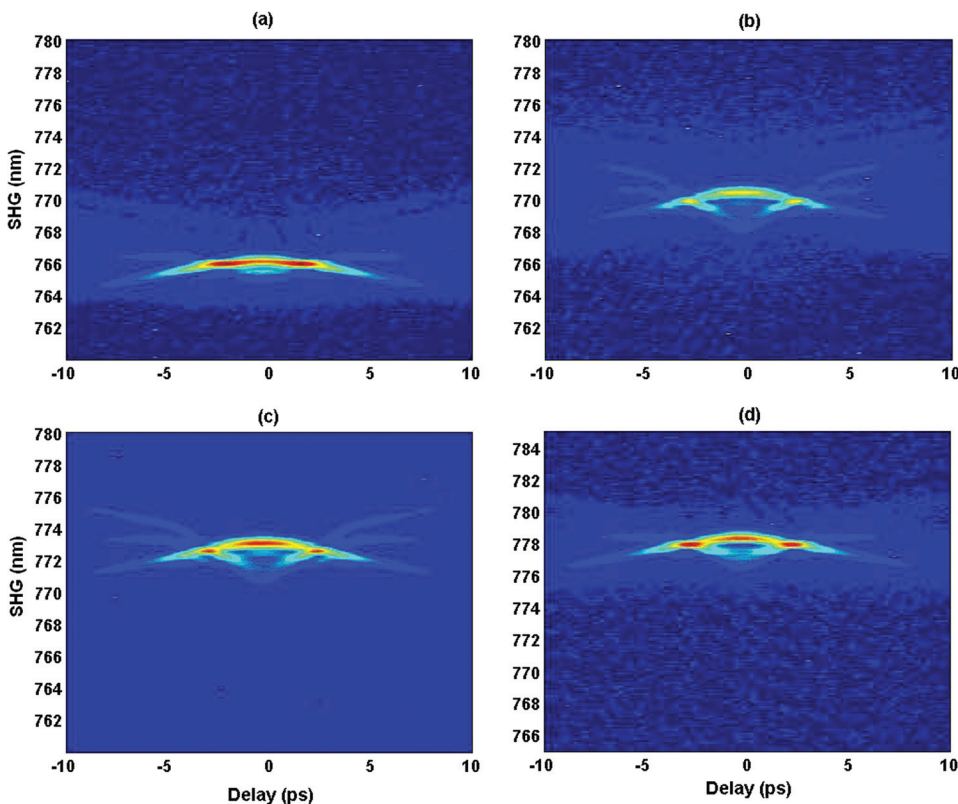


FIG. 2. Example 2D FROG spectrograms at the waveguide output for different center wavelengths. (a) 1535.98-nm; (b) 1544.14-nm; (c) 1549.79-nm; and (d) 1559.96-nm. Laser output pulse energies are 600 pJ in this example. Typical retrieved FROG error is approximately 1 to 2%.

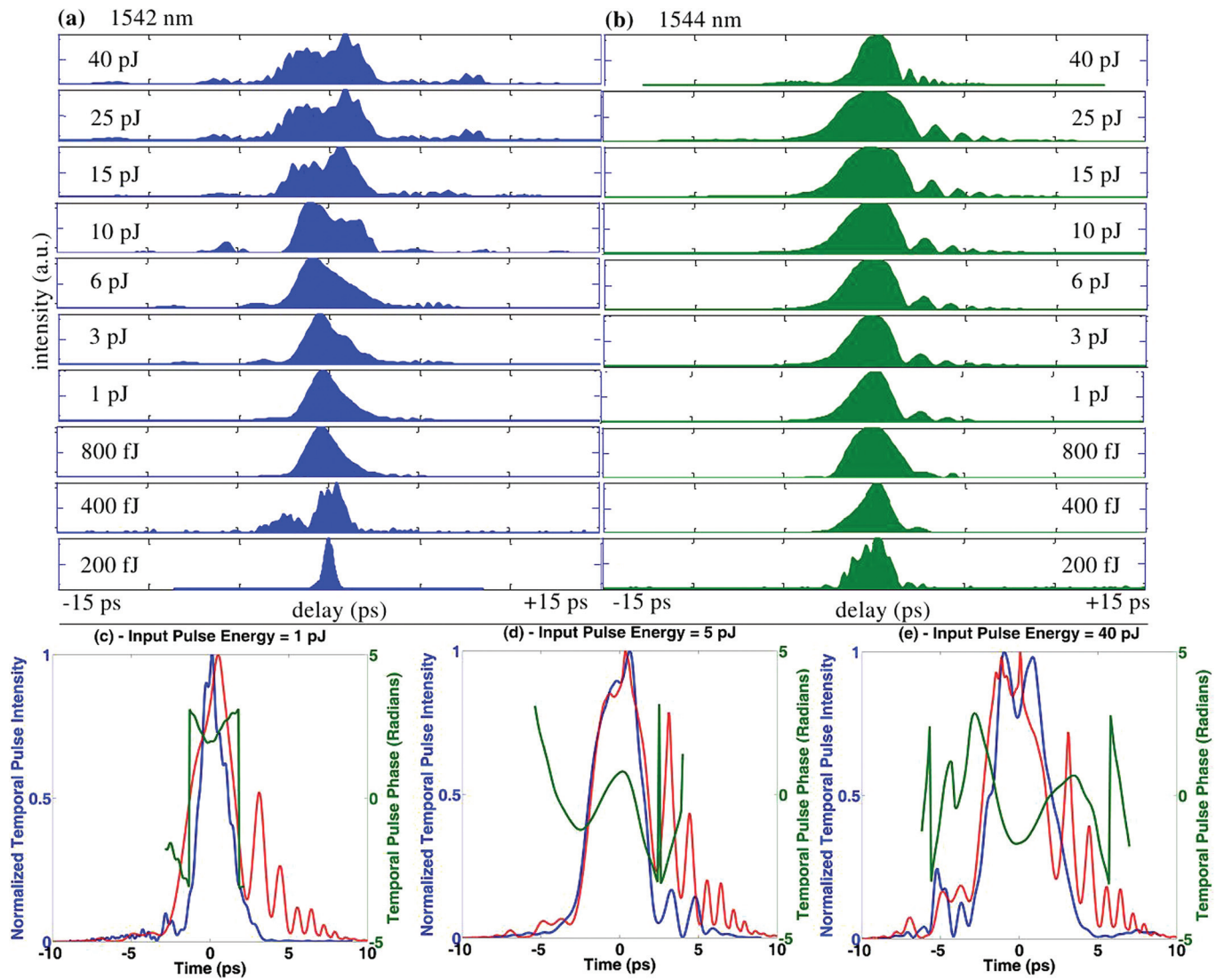


FIG. 3. FROG-retrieved parameters. (a) and (b) Pulse intensities with 1542 nm and 1544 nm pulse center wavelengths, respectively. The labels denote pulse energies at the waveguide input, with the waveguide output pulse energies and into the FROG at 10 to 15-dB lower. Retrieved pulse temporal phase (green line), retrieved pulse temporal intensity (blue line), and the numerically predicted NLSE pulse intensity (red line) after propagation in chip-scale waveguide at 1544-nm wavelength, for (c) 1 pJ, (d) 5 pJ, and (e) 40 pJ.

(χ_b of 1.2), and at 40-pJ (χ_b of 2-3), and some minor pulse splitting is observed. It should be noted that at these energies and the predicted chip dispersion, higher-order soliton numbers N (where N^2 is the ratio of the coupled soliton energy W to the fundamental soliton energy W_0) are calculated at 8, 19, and 54 for 1-pJ, 5-pJ, and 40-pJ pulse energies, respectively. Because of these high soliton numbers, pulse splitting could be expected, but also pulse compression. The broadening observed is evidence of other nonlinear phenomena at play.

To further understand the measurements, we concurrently perform nonlinear Schrödinger (NLSE) modeling of the optical pulse dynamics as illustrated in Figure 3(c). A split-step Fourier code was implemented to model the short pulse propagation^{22,23} in the semiconductor waveguide, along with Kerr, free-carrier absorption and dynamics, and two-photon absorption.^{24,25} The waveguide GVD β_2 was obtained numerically²⁶ and a consistent second order GVD of $-4.15 \text{ ps}^2/\text{m}$ used for our channel waveguide samples.²⁷ In addition, a third-order GVD of $+0.01 \text{ ps}^3/\text{m}$.²⁶ These values for the second and third order GVD were numerically

modeled for comparable silicon nanowire waveguides and are used consistently to model pulses of all the wavelengths measured. While in reality, there is always some change in GVD with change in wavelength, this was found to be negligible with these nanowire waveguides, especially when compared to the differences in TPA and free-carrier dynamics. Figures 3(c)–3(e) show a remarkable match between theory and experiment for the pulse intensities; the blue line represents the FROG measured pulse intensity, to compare with the red line representing the NLSE numerical results. For accuracy, the input pulse for the NLSE was the FROG measured pulse shape instead of a theoretical hyperbolic secant. The discrepancies with the temporal oscillations at the pulse trailing edge (positive delay) in the numerical simulations is due to the inherent fluctuations from the laser input, as each FROG measurement is averaged over many individual pulses.

Before we investigate our chip-scale measurements, we examine ideal soliton pulse compression within theoretical silicon waveguides. The fundamental soliton energy W_0 , for

a hyperbolic-secant solitary wave, is defined as $3.53\beta_2/(\gamma_{\text{eff}}T_{\text{FWHM}})$, where γ_{eff} is the third-order susceptibility Kerr-based parameter described by $(n_2\omega_o/cA_{\text{eff}}) \cdot (n_g/n_o)^2$, with n_2 the Kerr coefficient, ω_o the optical frequency, A_{eff} the effective waveguide area, and n_g and n_o the group and effective indices, respectively. For a 10-pJ and ~ 2.3 -ps pulses, this corresponds to an input soliton number N of 27, a dispersive length $L_d (=T_o^2/|\beta_2|)$ of 41 cm (sizably larger than our 4-mm sample length L), where $T_o = T_{\text{FWHM}}/\Gamma$ and $\Gamma = 1.76$ for ideal hyperbolic-secant pulses. The nonlinear length $L_{\text{NL}} (=1/\gamma_{\text{eff}}P_o)$ is $492 \mu\text{m}$, resulting in L_d/L_{NL} ratios in the range of 2580. Based on this estimates, the NLSE computations (Figure 4(a) inset) show possible pulse compression for 10-pJ 2.3-ps pulses, even in the presence of linear losses, two-photon and free-carrier absorption, with $7\times$ compression factor, albeit requiring 10-cm long waveguides based on the soliton period z_o . (Figure 4(a) inset is intensity normalized in the presence of linear and nonlinear losses.)

This numerical effort was conducted to verify the feasibility of soliton pulse compression in silicon nanowires, although with long waveguides. As a result, both linear and

nonlinear (TPA and FCA) losses are substantial, and the overall pulse attenuation is higher than can be practically observed in measurements. Second, with the longer lengths, lower energies are needed for the evolution of a soliton wave. Finally, this study utilized a consistent ideal pulse; in practice, this would not be achieved due to inherent minor variations in mode-locked lasers.

We also examine the pulse splitting with NLSE simulations. In periodic recurrence of higher-order solitons in the absence of TPA, pulse compression is often observed initially and followed by pulse splitting. SPM dominates initially, generating a frequency chirp for a red-shifted leading edge and a blue-shift trailing edge, with an accompanying spectral broadening. With the positively chirped pulse, anomalous dispersion then compresses the pulse and typically only in the pulse central region due to its linear chirp in this region. The compression in the central region changes the spectral character of the central lobe and results in, for example, a split-doublet spectrally. In our silicon medium, however, NLSE computations with only SPM and GVD as described above, and without TPA and free carrier dynamics,

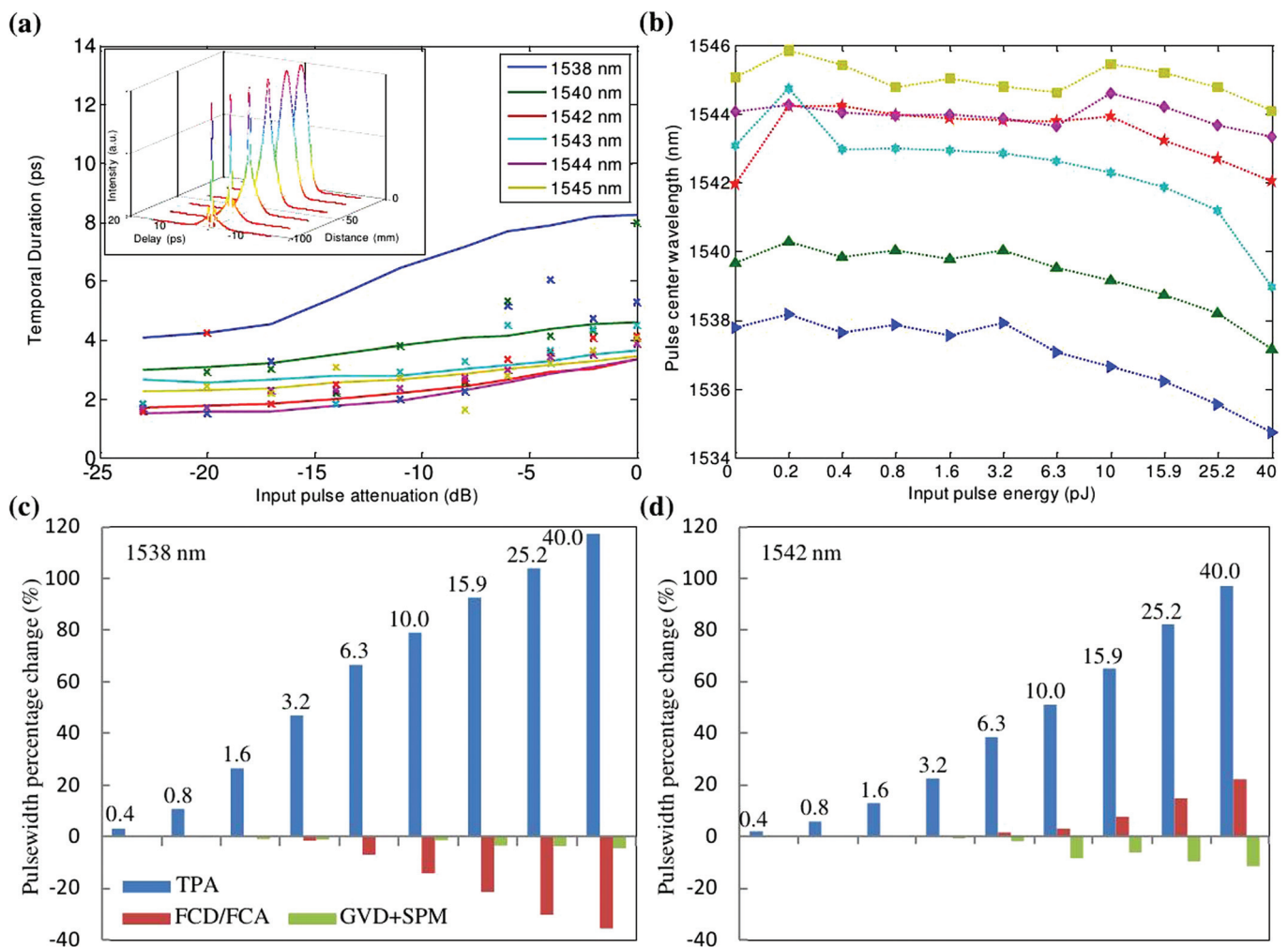


FIG. 4. Soliton pulse characteristics. (a) Output pulseduration versus input pulse energy, for different pulse center wavelengths. Inset: nonlinear Schrödinger model of pulse propagation in chip-scale waveguide, for 10-pJ and 2.3-ps input pulse. Measurements in data points and numerical simulations in solid lines. (b) Observed carrier blue-shift from plasma Drude dispersion. Color plot—wavelength assignment as in panel (a). Figures (c) and (d): Modeled relative contributions of isolated two-photon absorption (TPA), free-carrier dispersion (FCD), free-carrier dispersion absorption (FCA), group velocity dispersion (GVD), and self-phase modulation (SPM). Examined for increasing pulse energies (top labeled, in pJ), with 1538-nm and 1542-nm wavelengths, respectively. Positive percentage denotes pulse broadening, and percentage change is referenced to output pulseduration at low (200-fJ) pulse energy.

do not capture the temporal splitting shown in the FROG measurements [Figure 3(c) right-most panel]. Instead, when including the TPA and induced free-carrier dispersion and absorption, we observed a remarkable match between the FROG measurements and NLSE predictions.

Figure 4(a) summarizes the pulse broadening on-chip for the six example series of wavelengths and varying pulse energies. Dispersion across wavelengths is not large and typical pulse broadening up to twice the original pulse FWHM is observed both in the NLSE (solid lines) and measurements (data points). Though general pulse broadening is observed, we note that the broadening is not monotonic across the wavelengths due to slight changes in the input pulse between different center pulse wavelengths. In the NLSE modeling, the temporal widths were obtained by convolution and deconvolution of the pulse shape, a mathematical representation of the experimental temporal trace. We note there is good fit between theory and measurements, with the remaining discrepancies from numerical and group velocity dispersion imprecision.

Interestingly, we also observed an intensity-dependent blue-shift of the pulse central frequency as illustrated in Figure 4(b). Across the wavelengths, a blue-shift ranging between 0.74-nm to 4.13-nm was observed. This blue shift arises from the Drude plasma dispersion of two-photon excited free carriers,^{3,9,10,21} also captured in our full NLSE model with carrier dynamics. Figures 4(c) and 4(d) show the computed temporal pulsewidth change and relative contributions from TPA, free-carrier absorption and dispersion, SPM, and GVD. We examined this numerically for two example wavelengths, 1538-nm and 1542-nm. In both cases, the dominant process is TPA (in silicon) wherein the peak power is attenuated by the nonlinear absorption, leading to an attenuation of temporal pulse central region. We note that differences in the simulated free-carrier contribution is small and could be due to fluctuations in the input pulse character, taken from a single snapshot of the FROG measurement data. In both wavelengths, the percentage of ultrafast soliton compression on-chip from SPM and GVD is estimated to be small, mainly dominated by TPA.

In conclusion, we examined ultrafast pulse propagation and nonlinear dynamics in silicon waveguides, in both amplitude and phase. FROG measurements show temporal pulse broadening in our 4-mm waveguides and the onset of pulse splitting, with our 200-fJ to 40-pJ pulse energies. The numerical NLSE model illustrated the nonlinear pulse dynamics in our operating regimes, including two-photon and carrier effects, and matched remarkably the experimental measurements without any fitting. It was observed that at high energies, the TPA overcame the SPM, preventing soliton pulse compression and resulting in pulse broadening. This study supports the understanding of ultrafast nonlinear switching and optical processes in chip-scale information processing elements.

The authors acknowledge discussions with Alfredo de Rossi, Sylvain Combrié, Pierre Colman, James F. McMillan, Heng Zhou, Tingyi Gu, XinAn Xu, Pin-Chun Hsieh, Zhenda

Xie, Kishore Padmaraju, Noam Ophir, and the laboratory of Keren Bergman. The SEM images of Figure 1(a) are taken by James F. McMillan. This work was supported by the Navy Air Systems Command (NAVAIR)-4.0T Chief Technology Officer Organization as an Independent Laboratory In-House Research Basic Research Project, the Science Mathematics and Research for Transformation (SMART) fellowship, the National Science Foundation under award ECCS-1102257, and the National Science Foundation of China under award 61070040.

¹P. Colman, C. Husko, S. Combrie, I. Sagnes, C. W. Wong, and A. De Rossi, *Nature Photon.* **4**, 862 (2010).

²G. P. Agrawal, *Nonlinear Fiber Optics* (Academic Press, New York, NY, 2006).

³C. A. Husko, Ph.D. thesis, Columbia University, 2010.

⁴D. G. Ouzounov, F. R. Ahmad, D. Müller, N. Venkataraman, M. T. Gallagher, M. G. Thomas, J. Silcox, K. W. Koch, and A. L. Gaeta, *Science* **301**, 1702 (2003).

⁵D. T. H. Tan, P. C. Sun, and Y. Fainman, *Nature Commun.* **1**, 116 (2010).

⁶W. Ding, A. V. Gorbach, W. J. Wadsworth, J. C. Knight, D. V. Skryabin, M. J. Strain, M. Sorel, and R. M. De La Rue, *Opt. Express* **18**, 26625 (2010).

⁷J. I. Dadap, N. C. Panoiu, Xiaogang Chen, I-Wei Hsieh, Xiaoping Liu, Cheng-Yun Chou, E. Dulkeith, S. J. McNab, F. Xia, W. M. J. Green, L. Sekaric, Y. A. Vlasov, and R. M. Osgood, Jr., *Opt. Express* **16**, 1280 (2008).

⁸J. Zhang, Q. Lin, G. Piredda, R. W. Boyd, G. P. Agrawal, and P. M. Fauchet, *Opt. Express* **15**, 7682 (2007).

⁹L. Yin, Q. Lin, and G. P. Agrawal, *Opt. Lett.* **31**, 1295 (2006).

¹⁰L. Yin, Q. Lin, and G. P. Agrawal, *Opt. Lett.* **32**, 391 (2007).

¹¹C. J. Benton and D. V. Skryabin, *Opt. Express* **17**, 5879 (2009).

¹²N. Ophir, R. K. W. Lau, M. Menard, X. Zhu, K. Padmaraju, Y. Okawachi, R. Salem, M. Lipson, A. L. Gaeta, and K. Bergman, *Opt. Express* **20**, 6488 (2012).

¹³C. J. Chen, C. A. Husko, I. Meric, K. L. Shepard, C. W. Wong, W. M. J. Green, Y. A. Vlasov, and S. Assefa, *Appl. Phys. Lett.* **96**, 081107 (2010).

¹⁴P. Colman, S. Combrié, G. Lehoucq, A. de Rossi, and S. Trillo, *Phys. Rev. Lett.* **109**, 093901 (2012).

¹⁵B. Kibler, J. Fatome, C. Finot, G. Millot, F. Dias, G. Genty, N. Akhmediev, and J. M. Dudley, *Nature Phys.* **6**, 790 (2010).

¹⁶R. Trebino, *Frequency-resolved Optical Gating the Measurement of Ultrashort Laser Pulses* (Kluwer Academic Publishers, Norwell, MA, USA, 2000).

¹⁷A. Xing, Ph.D. thesis, University of California at Santa Barbara, 2005.

¹⁸S. Akturk, M. Kimmel, R. Trebino, S. Naumov, E. Sorokin, and I. Sorokina, *Opt. Express* **11**, 3461 (2003).

¹⁹Z. Wang, E. Zeek, R. Trebino, and P. Kvam, *Opt. Express* **11**, 3518 (2003).

²⁰C. Husko, S. Combrie, Q. V. Tran, F. Raineri, C. W. Wong, and A. De Rossi, "Non-trivial scaling of self-phase modulation and three-photon absorption in III-V photonic crystal waveguides," *Opt. Express* **17**, 22442 (2009).

²¹C. Husko, P. Colman, S. Combrié, A. De Rossi, and C. W. Wong, *Opt. Lett.* **36**, 2239 (2011).

²²N. C. Panoiu, J. F. McMillan, and C. W. Wong, *Appl. Phys. A* **103**, 835 (2011).

²³A. C. Peacock, N. Healy, J. R. Sparks, P. J. Sazio, and J. V. Badding, *Optics Letters* **35**, 3697 (2010).

²⁴T. Gu, N. Petrone, J. F. McMillan, A. van der Zande, M. Yu, G. Q. Lo, D. L. Kwong, J. Hone, and C. W. Wong, *Nature Photon.* **6**, 554 (2012).

²⁵C. A. Husko, A. de Rossi, S. Combrie, Q. V. Tran, F. Raineri, and C. W. Wong, *Appl. Phys. Lett.* **94**, 021111 (2009).

²⁶I.-W. Hsieh, X. Chen, J. I. Dadap, N. C. Panoiu, R. M. Osgood, Jr., S. J. McNab, and Y. A. Vlasov, *Opt. Express* **14**, 12380 (2006).

²⁷E. Dulkeith, F. Xia, L. Schares, W. M. J. Green, and Y. A. Vlasov, *Opt. Express* **14**, 3853 (2006).